Water-based and biocompatible 2D crystal inks for all-inkjet-printed heterostructures

Daryl McManus[1], Sandra Vranic[2], Freddie Withers[3], Veronica Sanchez-Romaguera[4],
Massimo Macucci[5], Huafeng Yang[1], Roberto Sorrentino[1], Khaled Parvez[1], Seok-Kyun Son[1],
Giuseppe Iannaccone[5], Kostas Kostarelos[2], Gianluca Fiori[5] and Cinzia Casiraghi[1]*

Exploiting the properties of two-dimensional crystals requires a mass production method able to produce heterostructures of arbitrary complexity on any substrate. Solution processing of graphene allows simple and low-cost techniques such as inkjet printing to be used for device fabrication. However, the available printable formulations are still far from ideal as they are either based on toxic solvents, have low concentration, or require time-consuming and expensive processing. In addition, none is suitable for thin-film heterostructure fabrication due to the re-mixing of different two-dimensional crystals leading to uncontrolled interfaces and poor device performance. Here, we show a general approach to achieve inkjet-printable, water-based, two-dimensional crystal formulations, which also provide optimal film formation for multi-stack fabrication. We show examples of all-inkjet-printed heterostructures, such as large-area arrays of photosensors on plastic and paper and programmable logic memory devices. Finally, *in vitro* dose-escalation cytotoxicity assays confirm the biocompatibility of the inks, extending their possible use to biomedical applications.

The electronics industry has been dominated by metals and complementary metal–oxide–semiconductor technology. However, constraints related to materials choice clearly appear in transparent and flexible electronics, heat management and rapid customization, all of which present challenges to traditional fabrication methods. An important advance was obtained with the introduction of conductive polymers[1], which allow simple, versatile and low-cost techniques, such as inkjet printing, to be used for the manufacture of functional devices[2–4].

The isolation of graphene[5] has unveiled a wide range of novel two-dimensional materials with outstanding properties[6–8]. This new class of materials shows great promise for use in flexible electronics, because their atomic thickness allows for maximum electrostatic control, optical transparency, sensitivity and mechanical flexibility[6,9]. In addition, because two-dimensional crystals are characterized by out-of-plane van der Waals interactions, they can be combined easily in one multilayer stack, offering unprecedented control of the properties and functionalities of the resulting heterostructure-based device[10]. In this framework, inkjet printing can provide an attractive route to low-cost and large-scale fabrication of heterostructures on any substrate. Furthermore, inkjet printing allows the fabrication of complex heterostructures, which can provide multiple functionalities and improved performance[11]. Methods such as vacuum filtration and spin/spray coating, which have been used previously for heterostructure fabrication[12,13], offer poor control of the thickness and roughness of the layers and have limited design flexibility.

Available inkjet printable formulations, produced by liquid-phase exfoliation[14], are still far from ideal as they are based on toxic and expensive solvents[15–17], require time-consuming and expensive formulation processing[18–22] or substrate functionalization[17], or need relatively high temperatures to dry[16,17], which

limits the range of substrates that can be used. In addition, none of these formulations is suitable for thin-film heterostructure fabrication, which requires multi-stack formation with well-defined interfaces. Fully printing a multilayer stack is a well-known challenge for printing technology[3,23]—the different materials in the stack tend to re-disperse at the interface, producing uncontrolled interfaces (Supplementary Fig. 2), resulting in poor device reproducibility and performance. Better control of interfacial effects and processing conditions allowed significant improvements in the performance of organic field-effect transistors[24].

Making new printable formulations of functional materials presents several challenges, as inkjet printing requires the ink to have specific physical properties[3,4]. Water, for example, is unsuitable for both liquid-phase exfoliation[14] and inkjet printing[4]. Surfactants can be added to water to both lower the surface tension and to stabilize the exfoliated nanosheets[25]. Such inks are not ideal for printed electronics, as they have a low concentration of two-dimensional crystals (<0.1 wt%)[26] and contain a high amount of residual surfactant. Other examples of printable water-based inks refer to graphene oxide or reduced-graphene oxide, which are defective and require additional thermal or chemical treatments.

In this Article we have developed a simple method for the production of highly concentrated, stable, inkjet-printable, water-based inks that can be formulated for a range of two-dimensional materials. No solvent exchange, chemical treatment or harsh conditions are used. The ink composition has been optimized to achieve optimal film deposition for multistack formation, allowing fabrication of all-inkjet-printed heterostructures, such as arrays of all-printed photosensors on plastic and programmable logic devices. Because the inks are expected to find utility in several applications as different consumer products, we also investigated possible

[1]School of Chemistry, University of Manchester, Manchester M13 9PL, UK. [2]Nanomedicine Lab, Faculty of Biology, Medicine and Health, AV Hill Building, University of Manchester, Manchester M13 9PT, UK. [3]School of Physics and Astronomy, University of Manchester, Manchester M13 9PL, UK. [4]Manchester Enterprise Centre, Alliance Manchester Business School, University of Manchester, Manchester M13 9SS, UK. [5]Dipartimento di Ingegneria dell'Informazione, Università di Pisa, Pisa, Italy. *e-mail: cinzia.casiraghi@manchester.ac.uk

Figure 1 | Range of inkjet-printable inks and their properties. a, Optical image of water-based two-dimensional crystal inks. Gr, graphene. **b,** Nobel medal printed with water-based graphene ink on PEL P60 paper. **c,** Printed 'MoS$_2$' with water-based MoS$_2$ ink on PEL P60 paper with an increasing number of printed passes (from 1 to 4, top to bottom). Note the relatively good contrast with the paper obtained even with one printed pass, due to the use of a highly concentrated ink. **d,** Optical picture of an array of all-printed Gr/WS$_2$/Gr heterostructures on PET. **e,** Sheet resistance as a function of thickness of the graphene lines (1 cm length) printed on Si/SiO$_2$, before and after annealing. Thickness data represent mean ± s.d. across a section of the printed line. Ink concentration is ~2 mg ml^{-1}, giving rise to a thickness of ~5 nm per print pass. The data are compared with the sheet resistance reported for NMP-based graphene inks from ref. 17. **f,** Sheet resistance for increasing number of printed passes for graphene lines (2 cm length) printed on PEL P60 paper (inset: optical images of printed lines made with 1, 5, 10, 15 and 20 printed passes, from bottom to top) with a drop spacing of 40 µm (red points). Note that in the case of paper, its porosity allows printing with small drop spacing (25 µm), leading to the deposition of a larger amount of material per unit area with fewer print passes, eventually minimizing R_s (blue points). Ink concentration, ~3 mg ml^{-1}.

adverse effects from exposure and determined their safety limitations by performing dose-escalation cytotoxicity assays *in vitro* using lung and skin cells.

Formulation engineering

Among steric and electrostatic stabilizers, pyrene sulfonic acid derivatives are able to produce concentrated, stable (up to one year) water-based two-dimensional crystal dispersions[27–29], characterized by a high graphene to stabilizer ratio compared to surfactants[30]. This exfoliation method has been shown to produce high-quality (that is, without oxygen-based groups) graphene dispersions[27]. However, these formulations are not inkjet-printable (Supplementary Fig. 1a) because an ink must have viscosity η, surface tension γ and density ρ within certain ranges for a set nozzle diameter α. The inverse Ohnesorge number Z is commonly used to predict if an ink will form stable drops: $Z = \sqrt{\gamma \rho \alpha}/\eta$ (ref. 31). The ink is expected to produce stable drops if $1 < Z < 14$ (ref. 31). For a nozzle diameter of 21.5 µm, Z is ~40 for water. To lower Z, the surface tension must be reduced and the viscosity increased using additives. Here triton x-100 was used to decrease the surface tension from ~73 to ~40 mN m^{-1}, and propylene glycol was used as co-solvent to increase the viscosity from 1 to 1.37 mPa s. This also disrupts the weak Marangoni flow, which helps reduce the coffee-ring effect[32]. These values of surface tension and viscosity give $Z \approx 20$ for the modified water-based ink. Despite $Z > 14$, the drop is stable, and no satellite drops or nozzle blocking are observed (Supplementary Movies 1 and 2). This is in agreement with water/ethylene glycol inks[33], which can be printed with $Z = 35.5$, and *N*-methyl-2-pyrrolidone (NMP)-based graphene inks, which show good printability with $Z > 20$ (refs 16,17).

Surfactant and co-solvent can be added before or after exfoliation of the bulk crystal. In this work we modify the dispersion after exfoliation. Note that we have never observed changes in concentration or stability (that is, re-aggregation), so the modification of the formulation does not alter the thickness distribution and quality of the flakes, as also confirmed by electrical measurements. Triton x-100, a non-ionic surfactant, was indeed chosen to avoid disrupting the electrostatic stabilization of graphene flakes provided by pyrene sulfonic acid derivatives.

The inks are shown in Fig. 1a. Several two-dimensional materials have been successfully exfoliated and printed, including graphene, MoS$_2$, WS$_2$ and hexagonal boron nitride (h-BN). Figure 1b,c shows some examples of printed patterns obtained with water-based graphene and MoS$_2$ inks, respectively, on PEL P60 paper. Other examples are provided in Supplementary Fig. 7. We point out that no treatment of the substrate is carried out, and the whole printing process is performed under ambient conditions. Figure 1e,f shows the values of the sheet resistance R_s of printed graphene lines on silicon (Si/SiO$_2$) and paper, respectively, for an increasing number of printed passes. R_s is infinite before the percolation threshold is reached[34], after which R_s decreases rapidly until the percolation-to-bulk threshold transition, at which point the graphene film behaves like a bulk material, with only small changes in sheet resistance resulting from each subsequent printing pass. The R_s values are comparable with literature results obtained for other types of printable graphene ink[16,17,19,35]. Thermal annealing at 300 °C for 1 h under a nitrogen atmosphere can be used to further lower R_s (Fig. 1e), but this process can be applied to a limited number of substrates, such as Si/SiO$_2$, quartz and polyimide.
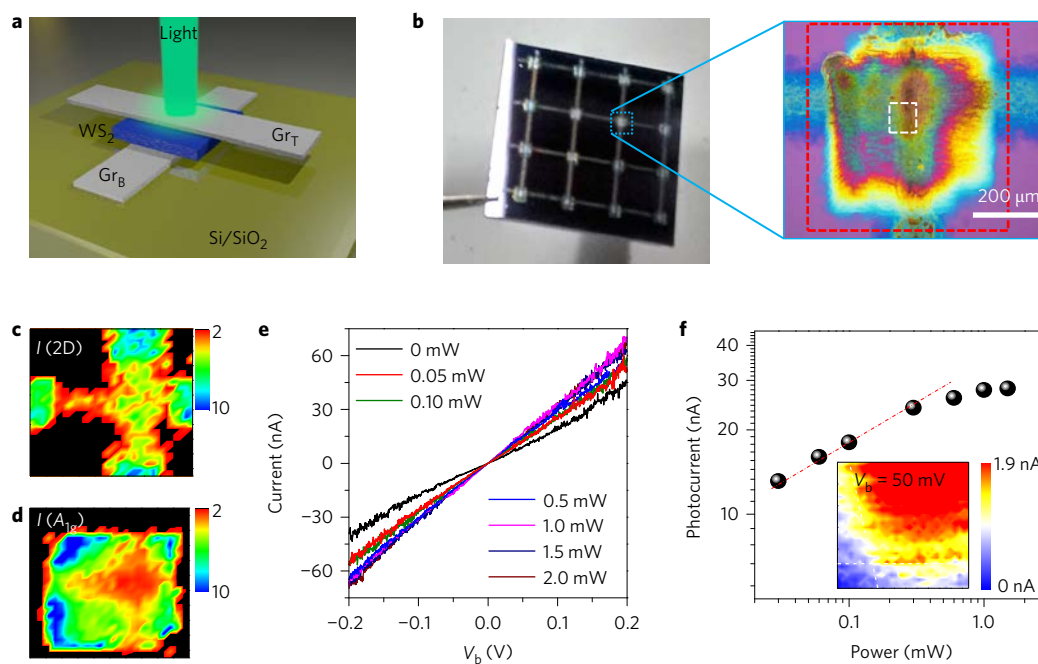
Figure 2 | Fully inkjet-printed heterostructures on Si/SiO$_2$. a, Schematic of an all-printed Gr$_B$/WS$_2$/Gr$_T$ heterostructure on a Si/SiO$_2$ substrate. **b**, Left: Optical picture of an array of 4 × 4 Gr$_B$/WS$_2$/Gr$_T$ heterostructures printed on Si/SiO$_2$. Right: Optical picture of one of the heterostructures, showing the two graphene electrodes and the square of photoactive material. **c,d**, Raman maps measured on the red dotted square (500 × 500 μm) in **b** (right) showing the intensity of the 2D peak (**c**) and the A_{1g} peak (**d**). **e**, I–V_b curves measured under different laser powers (at 488 nm). **f**, Photocurrent measured at V_b = 200 mV as a function of laser power. Inset: photocurrent map measured at V_b = 50 mV on the white dotted square in **b** (right). The red dashed line is a guide for the eyes.

Note that the thickness of the printed line varies as a function of ink concentration used. In the case of paper, its porosity allows fast drying, and thus printing with reduced drop spacing. By optimizing the drop spacing for a fixed ink concentration (2–3 mg ml^{-1}), we have been able to obtain R_s below 1 kΩ □$^{-1}$ above 40 printing passes (blue points, Fig. 1f). The thickness per pass on paper cannot be measured accurately due to the roughness of the substrate.

The basic ink formulation process can be further improved by removing excess pyrene after exfoliation with the use of a washing step. This allows us to increase the graphene concentration to 8 mg ml^{-1} (0.8 wt%), enabling graphene conductive lines to be printed with just one print pass. Single-pass printing is favourable as it allows reduced fabrication time and costs.

In printing technology it is common to modify a formulation to enhance some of its properties[3]. Here, we have added a binder to the modified formulation to minimize re-dispersion at the interface, allowing fabrication of all-printed heterostructures. The type and amount of binder depends on many factors[36]. In our case we chose polysaccharide xanthan gum because it is water-soluble, it acts as a binder, and only a low concentration is required to increase the viscosity. This allows retention of the electrical properties of the ink. Addition of the binder produces inks with non-Newtonian viscosity, that is, with shear-thinning properties, which helps form uniform lines, as the viscosity increases substantially after the droplets are deposited on the surface. A major advantage of xanthan gum over other binders is its biocompatibility[37]. Note that the binder can be added only after exfoliation as the high shear forces involved in exfoliation cause polymer degradation[38].

All-printed photodetectors

With this modified water-based ink we fabricated a heterostructure-based photodetector on a Si/SiO$_2$ substrate by printing a first graphene line of ~50 nm thickness at 50 °C. This acted as the bottom graphene electrode (Gr$_B$). A WS$_2$ square of ~100 nm

thickness, acting as the photoactive element, was then printed across the graphene line, and finally a second graphene line (~50 nm thickness) was printed perpendicular to the first, acting as top graphene electrode (Gr$_T$). The schematic of the Gr$_B$/WS$_2$/Gr$_T$ heterostructure is presented in Fig. 2a. Figure 2b (left panel) shows an optical picture of an array of 16 heterostructures on an area of 1 × 1 cm^2 on Si/SiO$_2$. Figure 2b (right panel) shows a high-magnification optical picture of one of the heterostructures. The appearance of interference colours is an indication of multi-stack formation. Raman mapping at 488 nm excitation wavelength was performed on the dotted red square in Fig. 2b (right). Figure 2c,d show the Raman maps of the intensity of the 2D peak of graphene and the A_{1g} peak of WS$_2$, respectively. This figure shows that the material has been deposited uniformly. After printing was completed, the sample was annealed under a N$_2$ atmosphere at 300 °C for 1 h to remove residual moisture. The nonlinear I–V curve in Fig. 2e confirms that multistacking layers were formed, with no bias voltage required for photocurrent response (Supplementary Section 4). Photocurrent mapping (Fig. 2f, inset) shows a uniform photocurrent response in the overlap region between the two graphene electrodes and the WS$_2$ square. The photocurrent efficiency of these printed devices is comparable with other heterostructures fabricated from inks using non-scalable methods[12]. Figure 2f also shows a power law for photocurrent versus laser power, which breaks at laser powers above ~0.5 mW. We found that all of the 16 heterostructures show the same I–V characteristic, within experimental error (for further data see Supplementary Section 4). Therefore, the device fabrication yield on Si/SiO$_2$ was found to be 100%.

An array of 20 Gr$_B$/WS$_2$/Gr$_T$ heterostructures were also printed onto polyethylene terephthalate (PET) film on an area of 3 × 4 cm^2 with no annealing (Fig. 1d). The I–V curves (Fig. 3a) show non-ohmic behaviour under no or little illumination, with a power law similar to that observed for the device in Fig. 2. Figure 3b shows that no photocurrent saturation is reached for laser powers up to ~3 mW (higher powers cause substrate degradation), in contrast to the device in
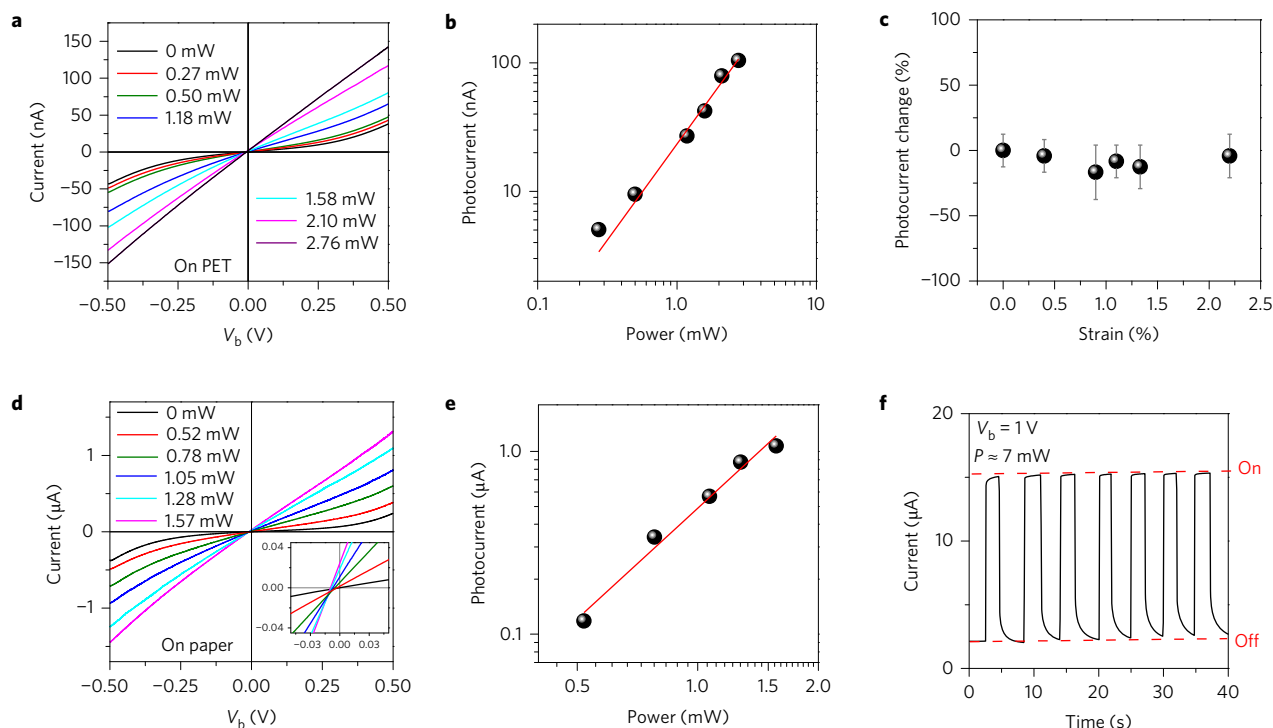
Figure 3 | Flexible heterostructures fully printed onto plastic and paper. a, I–V_b curves of an all-printed Gr_B/WS_2/Gr_T heterostructures on PET as a function of increasing laser power (λ = 514 nm). **b**, Photocurrent measured at V_b = 0.5 V and λ = 514 nm as a function of increasing laser power (the red line is an exponential fit of the experimental data). **c**, Bending test showing that the photocurrent of all-printed Gr_B/WS_2/Gr_T heterostructures on PET is stable up to ~2% strain. Data represent mean I_{OC} ± s.d. (n = 10). **d**, I–V_b curves of an all-printed Gr_B/WS_2/Gr_T heterostructure on paper as a function of increasing laser power (λ = 514 nm). Inset: Zoom on the data for V_b between –0.07 and 0.07 V to show changes in the short-circuit current with increasing laser power. **e**, Photocurrent measured at V_b = 0.5 V and λ = 514 nm as a function of increasing laser power (the red line is an exponential fit of the experimental data). **f**, Current generated by switching the laser source on and V_b = 1 V and laser power (P) of 7 mW. A photoresponsivity higher than 1 mA W^{-1} is obtained.

Fig. 2. This is due to the thicker Gr_T used in the case of the PET substrate, which decreases the effective laser power reaching WS_2. A bending test showed that the photocurrent is stable up to ~2% strain (Fig. 3c), in agreement with previous results reported for heterostructures made by inks[12]. Note that higher strain cannot be probed in our set-up due to damage of the silver contacts. It is also interesting to compare the conductivity of the devices in Figs 2 and 3a: the out-of-plane resistance is 3.8 MΩ at 1 V for the device in Fig. 2. The in-plane resistances range from 250 kΩ for Gr_B to 600 kΩ for Gr_T, and the larger resistance of Gr_T is probably due to the more uneven surface on which the top contact is printed (that is, on top of Gr_B and WS_2). Both values include contact resistance (~10 kΩ). For the device in Fig. 3a, the out-of-plane resistance is 13 MΩ at 0.5 V. Additional data are provided in Supplementary Fig. 14.

A simple way to improve device performance is to reduce the graphene resistance. This can be easily done by using graphene, grown by chemical vapour deposition, as Gr_B or Gr_T (Supplementary Fig. 12), or by maximizing the amount of material printed per unit area, either by increasing the ink concentration or by increasing the number of passes. With porous substrates such as paper, fast solvent absorption allows the drop spacing to be minimized during printing, which in turn increases the amount of material printed per unit area (Fig. 1f, blue data). Following this strategy, we fabricated a Gr_B/WS_2/Gr_T photodetector on paper (Supplementary Fig. 15). Figure 3d presents the I–V_b curves of the photosensor, where the resistance is observed to decrease with increasing laser power. Figure 3e shows the photocurrent measured at V_b = 0.5 V and λ = 514 nm as a function of increasing laser power. Figure 3f shows the current generated by switching the laser on and off every 10 s at V_b = 1 V. There is one order of magnitude increase in current when switching from off to on, giving rise to a responsivity

higher than 1 mA W^{-1}, well above the typical responsivity reported for devices made with liquid-phase-exfoliated two-dimensional crystals[12,16]. Note that for our devices a higher laser power can be used due to the increased thickness of the top graphene electrode.

All-printed read-only memories
The ability to design arbitrary arrays of heterostructures can be exploited to fabricate other types of device. Here, we show a programmable logic memory device made completely with two-dimensional crystals. Information storage is essential in any data-processing system. As a consequence, while pursuing the goal of obtaining an 'all-inkjet' printed circuit, we have to address the issue of implementing such an important building block.

For this purpose, we propose a programmable logic memory device enabled by inkjet printing technology, in which programming is performed at the time of fabrication. A 'word' is stored in the memory through the definition of a horizontal stripe ('word line') and vertical stripes, one for each bit of the word (which will be referred to as 'bit lines'), all made of graphene (Fig. 4a). A logic '1' is stored by short-circuiting the bit line to the word line, while a logic '0' is encoded by including a semiconducting layer (that is, WS_2) between the word line and the corresponding bit line, which eventually suppresses the current. In Fig. 4b, we show the fabricated device, including a schematic of the complete circuit set-up for the measurements, with the external bias voltage source V_P and load resistors R_L. When a voltage is applied to the word line (that is, 0.5 V), the stored word is read in terms of the voltage V_{Bi} across each pulldown resistor R_L, with higher voltage values (greater than 0.35 V) interpreted as logic '1' and lower voltage values (less than 0.135 V) as logic '0' (black solid line in Fig. 4c). In this specific case, the device is programmed with the word '010010001'. We
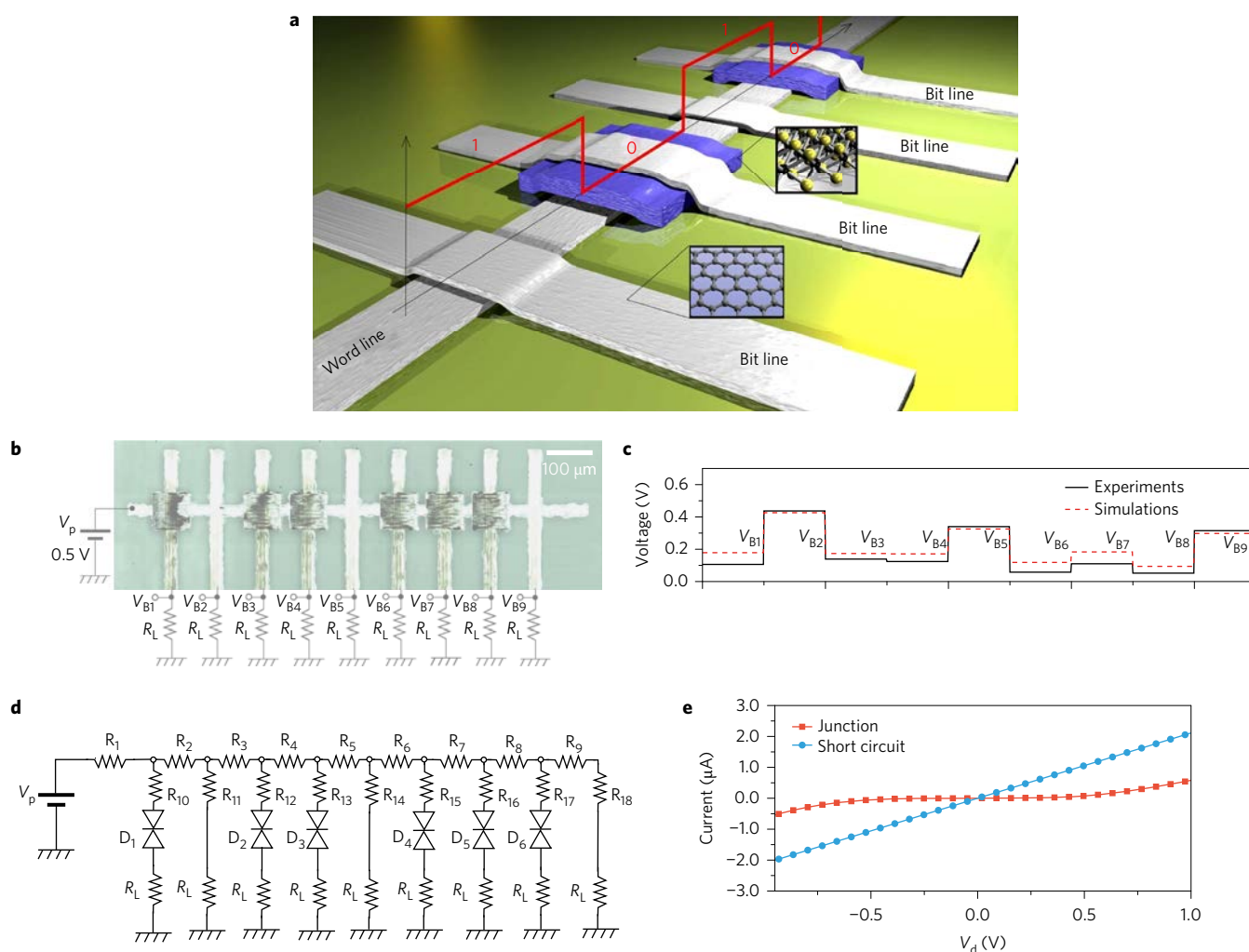
Figure 4 | Logic memory device. a, Sketch of the fabricated device. The programmable read only memory (PROM) is composed of a horizontal line (word line) and vertical lines (bit lines) made of ink-jet graphene. A logic '1' is stored at regular intersections of the word line and the bit line, while a logic '0' is programmed by printing WS_2 between the two. The sketch shows a 4-bit memory storing the word '1010'. **b**, Micrograph image of the fabricated device, with the bias voltage (V_p) source and load resistors (R_L) added. **c**, Experimental (black solid line) and simulated (red dashed line) results for operation of the circuit in **b**. **d**, Schematic of the equivalent electronic circuit. **e**, I–V characteristics of a graphene/WS_2/graphene junction and of a short circuit.

have also performed circuit simulations considering a distributed resistance for the graphene word and bit lines, and assuming that the graphene/WS_2/graphene junction (logic '0') behaves as an ambipolar device. In particular, the I–V characteristics have been extracted from the measurement performed on the circuit in Fig. 4b, and included into the industrial-grade electronic circuit simulator (in Fig. 4e we show an I–V characteristic of a junction as well as that of a short circuit). The simulation results of the equivalent circuit of Fig. 4b (Fig. 4d) are shown in Fig. 4c with red dashed lines and are in good agreement with experimental results.

The proposed device represents the first attempt to fabricate a memory with inkjet technology based on two-dimensional materials, and can be exploited in a wide range of applications. As an example, it could be included in printed radio-frequency identification tags to store an identification number. Note that the inclusion of additional elements in the device, such as diodes and transistors, would allow the device to perform more complex functions and increase the size of the read-only memory up to values of practical interest.

Biocompatibility studies on human cells

The potential adoption of two-dimensional crystal inks in a wide range of devices requires early determination of the risks associated with exposure of living organisms[39]. To offer an initial indication of the biocompatibility profile of these water-based inks, we conducted a series of cytotoxicity studies. We studied the response to dose-escalated ink exposure using cell culture models representative of the human tissues that constitute the primary physiological barriers in non-occupational (for example, skin exposure of consumers) and occupational (for example, pulmonary exposure of workers in the production lines of such materials) scenarios. The viability of human lung (human alveolar epithelial cells: A549) and skin (human keratinocytes: HaCaT) cells was assessed using two assays: the modified lactate dehydrogenase (LDH) assay—a colorimetric assay used to evaluate cellular membrane damage induced by the material—and propidium iodide (PI)/annexin V staining—used to distinguish cell viability by flow cytometry (fluorescence-activated cell sorting, FACS).

The modified LDH assay was developed[40] to avoid the potential false observations that are often reported as a result of interfering interactions between nanomaterials and reagents in colorimetric assays[41]. No differences in cell survival after 24 h of treatment with increased doses of the two-dimensional inks were observed compared to untreated cells (Fig. 5a,b). The LDH assay data were validated using FACS (Fig. 5c,d) by staining with cellular markers

5
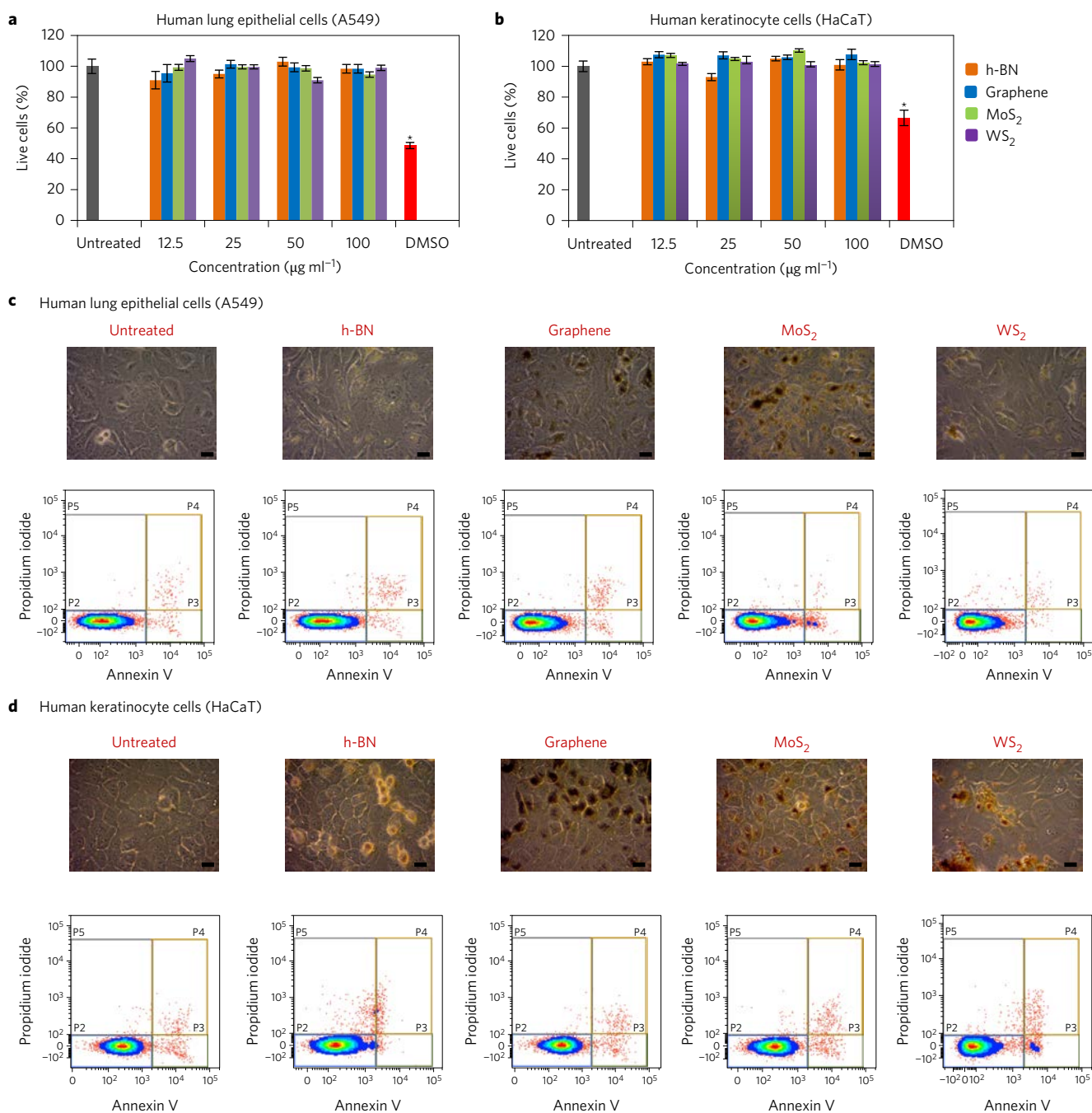
Figure 5 | Cytotoxic responses of human lung and keratinocyte cells to two-dimensional ink exposure. a,b, Cell membrane damage caused by the material in A549 (**a**) and HaCaT (**b**) cells assessed using the modified LDH assay. Cells were treated with escalating doses of h-BN, graphene, MoS_2 and WS_2 inks or 10% dimethyl sulfoxide (DMSO) for 24 h. Data are represented as mean ± s.d. ($n = 6$, error bars indicating variations inside each set of sextuplicates). Data were statistically analysed using analysis of variance (one-way ANOVA), with $P < 0.05$ considered significant. *Statistically different from untreated cells. **c,d**, Top row: Optical microscopy images of untreated cells and cells treated with 50 μg ml^{-1} of the inks for 24 h. Scale bars, 10 μm. Bottom row: Assessment of the cytotoxicity of the material by flow cytometry using PI/annexin V staining after incubation with the material for 24 h. In the bivariate plots, live cells are represented in the P2 region, early apoptotic are represented in the P3 region, late apoptotic and/or necrotic cells are shown in P4 region and necrotic cells are in the P5 region.

of apoptosis (annexin V) and necrosis (PI). Cells exhibiting different responses to two-dimensional ink exposure were gated according to healthy (unlabelled) cells (P2), early apoptotic (P3), late apoptotic and/or necrotic (P4) and necrotic cells (P5). Even at the highest dose of 100 μg ml^{-1}, cells appeared unstained, indicating the presence of predominantly alive cells (more than 90% of counted cells appeared in the P2 region; Supplementary Fig. 17). Overall, no significant cytotoxic responses compared to untreated cells were

observed at all doses (Supplementary Fig. 17). Optical microscopy of the two-dimensional ink-treated cell cultures (50 μg ml^{-1} for 24 h, Fig. 5c,d) indicated strong interactions between the material and cells, which can lead to binding and internalization; this is to be investigated further in future studies. In the present work, no significant morphological changes indicative of cell death were observed after treatment, such as decreased cellular confluence compared to the untreated cells, loss of cell/cell contact between

neighbouring cells, contracted nuclei or multinucleated giant cells. Overall, the modified LDH, FACS and microscopy data all indicated that the two-dimensional material used did not induce any significant cytotoxic responses in the two cell lines and the dose-escalation regime studied here.

So far, there have been very limited studies investigating the cytotoxic responses from exposure to exfoliated two-dimensional materials that can inform about any biocompatibility limitations. *In vitro* cytotoxic responses to MoS_2 nanosheets, using different exfoliating agents to the ones used in this study[42–44], have reported no significant adverse response using different cell lines. In another study the cytotoxic responses of A549 cells using different lithium-based exfoliating agents have been reported[45]. Similarly, the cytotoxic responses in HeLa (human cervical cancer cell line), 4T1 (mouse breast cancer cell line) and 293T (human embryonic kidney) cells to WS_2 nanosheets indicated that the type of exfoliating agent and their surface modifications play a critical role in induced cytotoxicity[46,47]. To determine thoroughly the biocompatibility profile of exfoliated two-dimensional nanosheets, more systematic studies should be performed. We have provided an initial comparative study among four types of two-dimensional inks and two human cell lines that indicate biocompatibility within the dose escalation studied here.

Conclusions

We have produced water-based, ink-jet-printable and biocompatible two-dimensional crystal inks that can find potential applications in smart packaging applications and identification tags, in particular for food, drinks, pharmaceuticals and consumer goods, where thinner, lighter, cheaper and easy-to-integrate components are needed.

Methods

Methods and any associated references are available in the online version of the paper.

References

1. Salaneck, W. R., Lundstrom, I., Huang, W. S. & Macdiarmid, A. G. A 2-dimensional surface-state diagram for polyaniline. *Synthet. Met.* **13,** 291–297 (1986).
2. Sirringhaus, H. *et al.* High-resolution inkjet printing of all-polymer transistor circuits. *Science* **290,** 2123–2126 (2000).
3. Baeg, K.-J., Caironi, M. & Noh, Y.-Y. Toward printed integrated circuits based on unipolar or ambipolar polymer semiconductors. *Adv. Mater.* **25,** 4210–4244 (2013).
4. Hutchings, I. M. & Martin, G. D. *Inkjet Technology for Digital Fabrication* Ch. 4 (Wiley, 2012).
5. Novoselov, K. S. *et al.* Two-dimensional atomic crystals. *Proc. Natl Acad. Sci. USA* **102,** 10451–10453 (2005).
6. Novoselov, K. S. *et al.* A roadmap for graphene. *Nature* **490,** 192–200 (2012).
7. Geim, A. K. Graphene: status and prospects. *Science* **324,** 1530–1534 (2009).
8. Geim, A. K. & Novoselov, K. S. The rise of graphene. *Nat. Mater.* **6,** 183–191 (2007).
9. Akinwande, D., Petrone, N. & Hone, J. Two-dimensional flexible nanoelectronics. *Nat. Commun.* **5,** 5678 (2014).
10. Geim, A. K. & Grigorieva, I. V. Van der Waals heterostructures. *Nature* **499,** 419–425 (2013).
11. Withers, F. *et al.* Light-emitting diodes by band-structure engineering in van der Waals heterostructures. *Nat. Mater.* **14,** 301–306 (2015).
12. Withers, F. *et al.* Heterostructures produced from nanosheet-based inks. *Nano Lett.* **14,** 3987–3992 (2014).
13. Kelly, A. G., Finn, D., Harvey, A., Hallam, T. & Coleman, J. N. All-printed capacitors from graphene-BN-graphene nanosheet heterostructures. *Appl. Phys. Lett.* **109,** 023107 (2016).
14. Hernandez, Y. *et al.* High-yield production of graphene by liquid-phase exfoliation of graphite. *Nat. Nanotech.* **3,** 563–568 (2008).
15. Coleman, J. N. *et al.* Two-dimensional nanosheets produced by liquid exfoliation of layered materials. *Science* **331,** 568–571 (2011).
16. Finn, D. J. *et al.* Inkjet deposition of liquid-exfoliated graphene and MoS_2 nanosheets for printed device applications. *J. Mater. Chem. C* **2,** 925–932 (2014).
17. Torrisi, F. *et al.* Inkjet-printed graphene electronics. *ACS Nano* **6,** 2992–3006 (2012).
18. Li, J. *et al.* Efficient inkjet printing of graphene. *Adv. Mater.* **25,** 3985–3992 (2013).
19. Secor, E. B., Prabhumirashi, P. L., Puntambekar, K., Geier, M. L. & Hersam, M. C. Inkjet printing of high conductivity, flexible graphene patterns. *J. Phys. Chem. Lett.* **4,** 1347–1351 (2013).
20. Yao, Y. High-concentration aqueous dispersions of MoS_2. *Adv. Funct. Mater.* **23,** 3577–3583 (2013).
21. Li, J., Naiini, M. M., Vaziri, S., Lemme, M. C. & Östling, M. Inkjet printing of MoS_2. *Adv. Funct. Mater.* **24,** 6524–6531 (2014).
22. Zheng, J. *et al.* High yield exfoliation of two-dimensional chalcogenides using sodium naphthalenide. *Nat. Commun.* **5,** 2995 (2014).
23. Gorter, H. *et al.* Toward inkjet printing of small molecule organic light emitting diodes. *Thin Solid Films* **532,** 11–15 (2013).
24. Gaikwad, A. M. *et al.* Identifying orthogonal solvents for solution processed organic transistors. *Org. Electron.* **30,** 18–29 (2016).
25. Lotya, M. *et al.* Liquid phase production of graphene by exfoliation of graphite in surfactant/water solutions. *J. Am. Chem. Soc.* **131,** 3611–3620 (2009).
26. Lotya, M., King, P. J., Khan, U., De, S. & Coleman, J. N. High-concentration, surfactant-stabilized graphene dispersions. *ACS Nano* **4,** 3155–3162 (2010).
27. Yang, H. *et al.* A simple method for graphene production based on exfoliation of graphite in water using 1-pyrenesulfonic acid sodium salt. *Carbon* **53,** 357–365 (2013).
28. Yang, H. *et al.* Dielectric nanosheets made by liquid-phase exfoliation in water and their use in graphene-based electronics. *2D Mater.* **1,** 1–10 (2014).
29. Schlierf, A. *et al.* Nanoscale insight into the exfoliation mechanism of graphene with organic dyes: effect of charge, dipole and molecular structure. *Nanoscale* **5,** 4205–4216 (2013).
30. Parviz, D. *et al.* Dispersions of non-covalently functionalized graphene with minimal stabilizer. *ACS Nano* **6,** 8857–8867 (2012).
31. Reis, N. & Derby, B. Ink jet deposition of ceramic suspensions: modeling and experiments of droplet formation. *MRS Online Proceeding Library Archive* **625,** 117–122 (2000).
32. Hu, H. & Larson, R. G. Marangoni effect reverses coffee-ring depositions. *J. Phys. Chem. B* **110,** 7090–7094 (2006).
33. Shin, P., Sung, J. & Lee, M. H. Control of droplet formation for low viscosity fluid by double waveforms applied to a piezoelectric inkjet nozzle. *Microelectron. Reliab.* **51,** 797–804 (2011).
34. Stauffer, D. & Aharony, A. *Introduction To Percolation Theory* Ch. 5 (Taylor & Francis, 1994).
35. De, S. & Coleman, J. N. Are there fundamental limitations on the sheet resistance and transmittance of thin graphene films? *ACS Nano* **4,** 2713–2720 (2010).
36. Secor, E. B. & Hersam, M. C. Emerging carbon and post-carbon nanomaterial inks for printed electronics. *J. Phys. Chem. Lett.* **6,** 620–626 (2015).
37. Eastwood, M. A., Brydon, W. G. & Anderson, D. M. The dietary effects of xanthan gum in man. *Food Addit. Contam.* **4,** 17–26 (1987).
38. Wheeler, J. S. R. *et al.* Effect of polymer branching on degradation during inkjet printing. *Polym. Degrad. Stab.* **128,** 1–7 (2016).
39. Kostarelos, K. & Novoselov, K. S. Graphene devices for life. *Nat. Nanotech.* **9,** 744–745 (2014).
40. Ali-Boucetta, H., Al-Jamal, K. T. & Kostarelos, K. Cytotoxic assessment of carbon nanotube interaction with cell cultures. *Methods Mol. Biol.* **726,** 299–312 (2011).
41. Latiff, N. *et al.* Toxicity of layered semiconductor chalcogenides: beware of interferences. *RSC Adv.* **5,** 67485–67492 (2015).
42. Shah, P., Narayanan, T. N., Li, C. Z. & Alwarappan, S. Probing the biocompatibility of MoS_2 nanosheets by cytotoxicity assay and electrical impedance spectroscopy. *Nanotechnology* **26,** 1–7 (2015).
43. Wang, X. *et al.* Differences in the toxicological potential of 2D versus aggregated molybdenum disulfide in the lung. *Small* **11,** 5079–5087 (2015).
44. Teo, W. Z., Chng, E. L., Sofer, Z. & Pumera, M. Cytotoxicity of exfoliated transition-metal dichalcogenides (MoS_2, WS_2, and WSe_2) is lower than that of graphene and its analogues. *Chem. Eur. J.* **20,** 9627–9632 (2014).
45. Chng, E. L., Sofer, Z. & Pumera, M. MoS_2 exhibits stronger toxicity with increased exfoliation. *Nanoscale* **6,** 14412–14418 (2014).
46. Yong, Y. *et al.* WS_2 nanosheet as a new photosensitizer carrier for combined photodynamic and photothermal therapy of cancer cells. *Nanoscale* **6,** 10394–10403 (2014).
47. Cheng, L. *et al.* PEGylated WS_2 nanosheets as a multifunctional theranostic agent for *in vivo* dual-modal CT/photoacoustic imaging guided photothermal therapy. *Adv. Mater.* **26,** 1886–1893 (2014).

Author contributions

C.C. conceived and designed the experiments. D.M.M. developed the inks, with initial assistance from V.S.-R., and conducted all experiments. H.Y. and R.S. performed preliminary experiments. K.P. contributed to the electrical measurements data. S.-K.S. contributed to the transfer of CVD graphene. Device characterization was performed by F. W. and D.M.M. G.F. and G.I. conceived the logic memory device with assistance from C.C. The device was fabricated by D.M.M. and measured by M.M. All biological studies were conceived, designed and performed by S.V. and K.K. The manuscript was written by C.C., D.M.M., G.F., S.V. and K.K., in close consultation with all authors.

Additional information

Supplementary information is available in the online version of the paper. Reprints and permissions information is available online at www.nature.com/reprints. Correspondence and requests for materials should be addressed to C.C.

Competing financial interests

The authors declare no competing financial interests.

Methods

Ink preparation. Graphite (99.5% grade) was purchased from Graphexel. All co-solvents, Triton x-100 and xanthan gum were purchased from Sigma-Aldrich. Dimatix cartridges (10 μl) and PEL P60 paper were purchased from Printed Electronics. Si/SiO$_2$ wafers were obtained from IDB Technologies. CVD graphene was purchased from 2D-Tech. The dispersion was sonicated at 300 W using a Hilsonic bath sonicator for 72 h. Flakes of the appropriate lateral size were collected via differential centrifugation to reduce the chance of nozzle blockages. The liquid obtained was centrifuged using a Sigma 1–14k refrigerated centrifuge at 903g for 20 min before collecting the supernatant. The collected supernatant was then centrifuged at 16,600g for 1 h and the precipitate re-dispersed in the printing solvent. The solvent consisted of less than 1:10 propylene glycol:water by mass, ≥0.06 mg ml^{-1} Triton x-100 and ≥0.1 mg ml^{-1} xanthan gum. The concentration of two-dimensional material was determined by UV–vis spectroscopy, and the rheological properties were studied before printing (Supplementary Sections 1 and 2). The lateral size of the nanosheets was characterized by atomic force microscopy (Supplementary Fig. 5). No aggregation was observed when the ink was transferred in the cartridge or during printing. More details are provided in Supplementary Sections 2 and 3.

Printing. A Dimatix DMP-2800 inkjet printer (Fujifilm Dimatix) was used; this can create and define patterns over an area of about 200 × 300 mm^2 and handle substrates up to 25 mm thick. The nozzle plate consisted of a single row of 16 nozzles of 23 μm diameter spaced 254 μm apart, with a typical drop size of 10 pl. Inks are printed onto a variety of substrates, including Si/SiO$_2$ (290 nm thermally grown oxide layer), SiO$_2$ (Quartz), PEL P60 paper and CVD graphene. The printed features were characterized by optical microscopy, Raman spectroscopy and atomic force microscopy (Supplementary Section 3). Sheet resistance was measured with two contact probes and included contact resistance.

Photocurrent measurements. Photocurrent maps were collected using a WiTEC Alpha 300 confocal Raman microscope equipped with 488, 514.5 and 633 nm excitation wavelengths. Laser power was measured by a Thorlabs PM100D optical power meter. A bias voltage was applied using a Keithley 2614B sourcemeter, which was also used to record *I–V* curves of the photoactive elements. The optically induced voltage change was measured across a 1 kΩ resistor by a Keithley 2182A voltmeter and relayed into the WiTEC control software to generate a photocurrent map. A National Instruments LabVIEW 2015 was used to control the sourcemeter and record data.

Cell culture. Human epithelial lung carcinoma cells (A549, ATCC, CCL-185) were maintained in Nutrient Mix F12 Ham medium (Sigma-Aldrich) supplemented with 10% FBS (Thermo Scientific), 50 μg ml^{-1} penicillin, 50 μg ml^{-1} streptomycin (Sigma-Aldrich) at 37 °C in 5% CO$_2$. Human keratinocyte cells (HaCaT) were provided by S. Pilkington (Department of Dermatology, University of Manchester) and were maintained in DMEM medium (Sigma-Aldrich) supplemented with 10% FBS, 50 μg ml^{-1} penicillin, 50 μg ml^{-1} streptomycin at 37 °C in 5% CO$_2$. Both cell lines were authenticated by sequencing (using polymorphic short tandem repeat loci) and have been independently tested to confirm the absence of mycoplasma contamination (Supplementary Fig. 18).

Cell culture treatment. Depending on the experiment, cells were seeded in 96 (LDH assay) or 12 (FACS analysis) well plates (Costar, Sigma) and treated when 70–80% confluence was reached. All treatments were performed in the cell culture medium in the absence of FBS, and 10% FBS was added to each well 4 h after treatment. h-BN (1.6 mg ml^{-1}), graphene (5.84 mg ml^{-1}), MoS$_2$ (1.44 mg ml^{-1}) and WS$_2$ (0.5 mg ml^{-1}) were vortexed shortly before making final dilutions for the treatment in the corresponding cell culture medium. Cells were exposed to 12.5–25–50–100 μg ml^{-1} h-BN, graphene, MoS$_2$ or WS$_2$ material for 24 h. Solvent (containing 0.06 mg ml^{-1} Triton x-100), used to stabilize the inks, was also tested for its toxicity using 0.012–0.006–0.003–0.0015 mg ml^{-1} Triton x-100, corresponding to the 100–50–25–12.5 μg ml^{-1} WS$_2$ inks.

Annexin V–Alexa Fluor 488 conjugate/PI assay. After 24 h of treatment at the indicated concentrations, cells were gently washed three times with PBS Ca^{2+}/Mg^{2+} (Sigma-Aldrich). Annexin-V staining was performed according to the manufacturer's instructions (Thermo Fisher Scientific). A total of 10,000 cells were analysed on a BD FACSVerseTM flow cytometer using 488 nm excitation and 515 and 615 nm band-pass filters for annexin V and PI detection, respectively. Material alone (without cells) was analysed in order to set up the gates including cell population for the analysis.

Modified LDH assay. The LDH assay was modified to avoid any interference from interactions of the material with the assay[40]. Briefly, the LDH content was assessed in intact cells that survived the treatment, instead of detecting the amount of LDH released in the medium upon treatment, using the following equation:

$$\text{Cell survival}\% = \left[\left(\alpha_{490\,\text{nm}}\text{of treated cells}\right)/\left(\alpha_{490\,\text{nm}}\text{of untreated cells}\right)\right] \times 100 \quad (1)$$

The absorbance α was read at 490 nm using a plate reader. The amount of LDH detected represented the number of cells that survived the treatment.